Electrochimica Acta 56 (2011) 4638–4644

Contents lists available at ScienceDirect

Electrochimica Acta

journal homepage: www.elsevier.com/locate/electacta

Synthesis and characterization of electrodeposited samaria and samaria-doped ceria thin films

V. Lair[a,*], L.S. Živković[a,b], O. Lupan[a,c], A. Ringuedé[a]

[a] Laboratoire d'Electrochimie, Chimie des Interfaces et Modélisation pour l'Énergie, LECIME, CNRS UMR 7575-ENSCP Chimie Paristech, 11rue Pierre et Marie Curie, 75231 Paris cedex 05, France
[b] The Vinča Institute of Nuclear Sciences, University of Belgrade, PO Box 522, 11 001Belgrade, Serbia
[c] Department of Microelectronics and Semiconductor Devices, Technical University of Moldova, 168 Stefan cel Mare Blvd., Chisinau, MD-2004, Republic of Moldova

ARTICLE INFO

Article history:
Received 3 December 2010
Received in revised form 23 February 2011
Accepted 24 February 2011
Available online 2 March 2011

Keywords:
Electrodeposition
Samaria (Sm_2O_3)
Samaria-doped ceria (SDC)
Cathodic electrodeposition
Thin film
Nanostructure
SOFC

ABSTRACT

Samaria (Sm_2O_3) and samaria-doped ceria (SDC) films are electrochemically deposited on stainless steel in view of a potential use in solid oxide fuel cells. As it is possible to deposit separately pure ceria (CeO_2) and pure samaria (Sm_2O_3) in similar conditions, SDC films were successfully obtained in one electrochemical conditions set. Thin films have been fabricated at low-temperature (30 °C) by applying a cathodic potential of −0.8 V/SCE, for 2 h. Structural and morphological properties of electrodeposited films have been studied by X-ray diffraction (XRD), scanning electron microscopy (SEM), techniques and Raman spectroscopy. Special attention has been focused on the Raman spectroscopy study to emphasize the effect of heat treatment and samarium doping. Despite cracks, single SDC phase was obtained crystallizing in a cubic symmetry.

1. Introduction

Pure and rare-earth containing ceria (CeO_2) have been extensively investigated for various technological applications. Indeed, due to their ability to store, release or transport oxygen, these materials have been widely used in catalytic fields as hydrocarbon oxidation catalysts, gas sensors, or in water gas shift reactions [1–4]. In solid oxide fuel cells (SOFCs), ceria-based materials could find several applications such as electrolyte [5] or interfacial layer as diffusion barrier [6] or as a bond layer [7]. One of the main advantages of doped ceria solid electrolytes over well-known yttria-stabilized zirconia is their ability to lower the operation temperature of SOFCs, due to their higher ionic conductivity at lower temperature [8,9]. Aliovalent substitution of trivalent ions in the lattice of ceria, results in the formation of oxygen vacancies and giving rise to an increase in ionic conductivity. The highest formation of oxygen vacancies was observed for $Ce_{1-x}Sm_xO_{2-x/2}$ and $Ce_{1-x}Gd_xO_{2-x/2}$ [10,11]. Therefore, lowering the SOFC working temperatures to 500–650 °C could allow greater flexibility in designing electrode and interconnecting materials. Conventional lanthanum chromite interconnectors may be replaced by much cheaper, well-adapted, stainless steel ones. However, to avoid added electrical resistance or alloy constituent diffusion from stainless steel to the cathode, it is necessary to protect the interconnect plates [8,12]. Ceria-based thin layer seems to be one of the solutions, when doped with respective element.

In the past decades, CeO_2-based coatings have been regarded as a possible, environmentally friendly, alternative to highly toxic chromate coatings for protecting structural materials (Al-alloys, zinc, stainless steel) [13–15]. CeO_2 films impair corrosion protection as anti-corrosion dopants [16] or surface conversion layers [17,18], because lanthanides block cathodic sites of the substrate [19]. Ceria coatings have also been used for enhancing corrosion resistance of the Mg-implants [20].

Samarium is another rare-earth element that, in close analogy with the behavior of cerium, also forms thin films capable of protecting the metallic substrates from corrosion attack [21]. Electrodeposition is a powerful cost-effective technique, which enables the production of high-quality coatings at low temperature. The method is highly versatile; one can play on a large variety of growth parameters to control the film properties. A number of reports were devoted to electrochemically synthesized ceria films [22–27]. Our team also reported on the synthesis of undoped ceria film [28–30]. However, the electrodeposition mechanisms for obtaining samarium-doped ceria films is still poorly documented, only a few studies may be found to our knowledge [14,31,32]. Recently, Ruiz

* Corresponding author.
E-mail address: virginie-lair@ens.chimie-paristech.fr (V. Lair).

0013-4686/$ – see front matter © 2011 Elsevier Ltd. All rights reserved.
doi:10.1016/j.electacta.2011.02.101

et al. [21] demonstrated the formation mechanism of samarium based-coatings to be similar to the ceria one. Most of the above-mentioned studies were carried out via a galvanostatic method.

In this work, samaria and samaria-doped ceria thin films have been grown using electrochemical deposition method under potentiostatic mode. In view of the potential application, as protective coatings against the corrosion of bipolar plates in high temperature fuel cell, samaria and SDC films have been deposited on stainless steel, from aqueous electrolytic solutions at 30 °C. This temperature has been chosen in order to improve the adherence of the ceria-based film. Moreover Hamlaoui et al. have recently shown that higher temperatures lead to film properties not adequate for protection [33]. Electrochemical behavior of the Sm^{3+} and Ce^{3+} systems has been investigated by means of cyclic voltammetry. A detailed analysis of structural, morphological and vibrational characteristics of the as-grown films is presented. Moreover, the effect of thermal annealing has been studied as well, with the aim of following the evolution of the crystal structure of samaria and samaria-doped ceria films.

2. Experimental

A classical three-electrode cell was used for the electrodeposition: stainless steel disc (316 L, diameter 0.7 cm) as a working electrode (kept under stirring at 300 rpm), saturated calomel electrode (SCE, E_{SCE} = 0.245 V vs. ENH) as the reference one, and platinum wire as a counter electrode. The substrate was abraded with SiC 800 paper, then cleaned for 5 min in ethanol under ultrasonics, rinsed with deionized water (electrical resistivity 18.2 MΩ cm), and dried under pulsed air flux immediately before deposition. The supporting electrolyte was 0.1 M $NaNO_3$ (Riedel de Haen). Then, three deposition media were investigated:

- for the fabrication of samaria films, the electrolytic solution contained 1 mM $Sm(NO_3)_3{\cdot}6H_2O$ (Alfa Aesar, 99.9%) in addition to the supporting electrolyte.
- for the synthesis of ceria films, 0.05 M $Ce(NO_3)_3{\cdot}6H_20$ (Alfa Aesar) were added to the supporting electrolyte.
- for the samaria doped ceria films, the solution bath contained the supporting electrolyte, and both $Ce(NO_3)_3{\cdot}6H_20$ (Alfa Aesar) and $Sm(NO_3)_3{\cdot}6H_20$ in order to obtain 0.8% Sm(III) calculated on the Ce(III) molar basis (see [34] for further details).

All the solutions were saturated with molecular oxygen for 1 h before starting the experiment, and slight O_2 bubbling in the reactor bath was maintained during the deposition. The bath temperature was kept at 30 °C using a bain-marie system, with a hot plate and thermal regulation. Films were deposited in a potentiostatic mode, applying a −0.8 V vs. SCE potential for 2 h. A Princeton Applied Research potentiostat/galvanostat (model 263A) was used. After electrodeposition the as-grown coatings were rinsed in deionized water. Thermal annealing was done in a tubular furnace at 600 °C for 1 h, in air, with a heating rate of 2 °C per minute. XRD analysis was performed using a Siemens D5000 XRD unit (with 40 kV and 45 mA, CuKα radiation with λ = 0.15406 nm) in θ–2θ range of 10°–100°. X'pert Database 32 software with integrated Scherrer formula was used to calculate the average crystallite size. SEM images were obtained by a high resolution Ultra 55 Zeiss FEG scanning electron microscope at an acceleration voltage of 10 kV. Energy dispersive X-ray (EDX) analyses were made using a Bruker Li-drift silicon detector, with a 15 kV acceleration voltage. Micro-Raman spectra were recorded at room temperature with a Horiba Jobin system at a spatial resolution of 2 μm in a backscattering configuration. A 632.8 nm line of a He–Ne laser was used for off-resonance excitation. The instrument was calibrated to the same accuracy using a naphtalene standard. Cyclic voltammetry (CV) experiments were carried out in the potential range (*E*) from +0.2 to −1.2 V vs. SCE, and scanning rate of 50 mV s^{-1}.

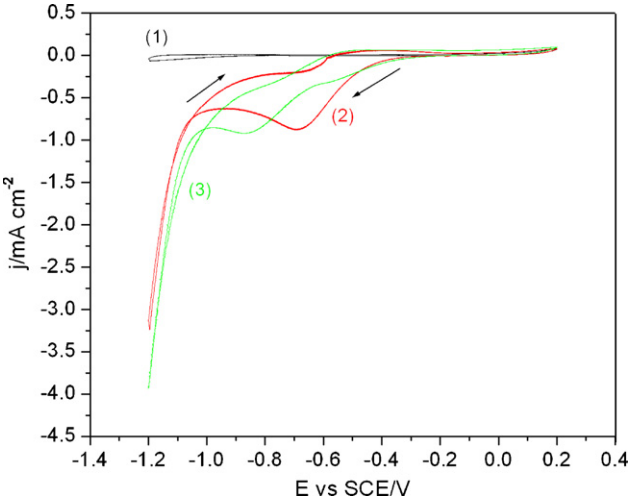

Fig. 1. Cyclic-voltammograms (CV) on stainless steel electrode in 0.1 M $NaNO_3$ solution (scanning rate 50 mV s^{-1}): curve (1) under Ar, curve (2) under oxygen, and curve (3) upon addition of 0.001 M Sm^{3+} under oxygen.

3. Results and discussion

3.1. Electrochemical deposition in the Sm(III) and Ce(III)/Sm(III) system.

The mechanism of electrochemical deposition is based on the generation of hydroxide ions (OH^-) by reduction of a soluble precursor on the conductive substrate, which acts as the working electrode. Then, the OH^- ions, produced in the vicinity of the working electrode, react with the metal cations present in the solution to form the oxide thin film on the electrode surface [24,35].

In the case of cerium ions and using molecular oxygen as a precursor, the deposition reactions can be written as follows:

$$1/2O_2 + H_2O + 2e^- \rightarrow 2OH^- \quad (1)$$

$$Ce^{3+} + 3OH^- \rightarrow Ce(OH)_3 \quad (2)$$

$$4Ce^{3+} + O_2 + 4OH^- + 2H_2O \rightarrow 4Ce(OH)_2{}^{2+} \quad (3)$$

The cerium oxide film results from either oxidation of $Ce(OH)_3$ or hydrolysis of $Ce(OH)_2{}^{2+}$, Eqs. (4) and (5), respectively [20,25,27]:

$$Ce(OH)_3 \rightarrow CeO_2 + H_3O^+ + e^- \quad (4)$$

$$Ce(OH)_2{}^{2+} + 2OH^- \rightarrow CeO_2 + 2H_2O \quad (5)$$

This method can potentially be extended to other lanthanide oxides [21,36]. In the case of Sm^{3+} ions, the expected reaction is the formation of samarium hydroxide:

$$Sm^{3+} + 3OH^- \rightarrow Sm(OH)_3 \quad (6)$$

The alternative product could be samarium oxide:

$$Sm^{3+} + 3OH^- \rightarrow 1/2Sm_2O_3 + 3/2H_2O \quad (7)$$

First deposition experiments were devoted to the study of pure samaria films grown on a stainless steel substrate. In order to select an appropriate deposition potential, electrochemical behavior of the system containing $Sm(NO_3)_3$ was investigated by means of cyclic voltammetry. Fig. 1 shows typical cyclic-voltammograms (CV) of the real stainless steel-electrolyte interface recorded upon a first voltammetry scan on the bare stainless steel electrode.

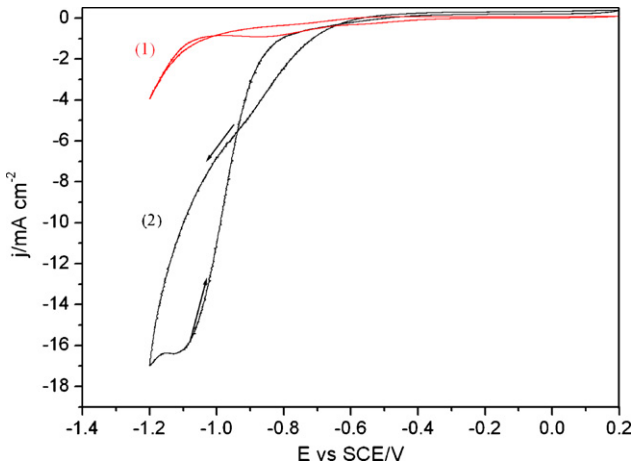

Fig. 2. Cyclic-voltammograms (CV) on stainless steel electrode in 0.1 M $NaNO_3$ solution, under O_2 (scanning rate 50 mV s^{-1}) (1) addition of Ce^{3+} 0.05 M. (2) Addition of Sm^{3+} 0.001 M.

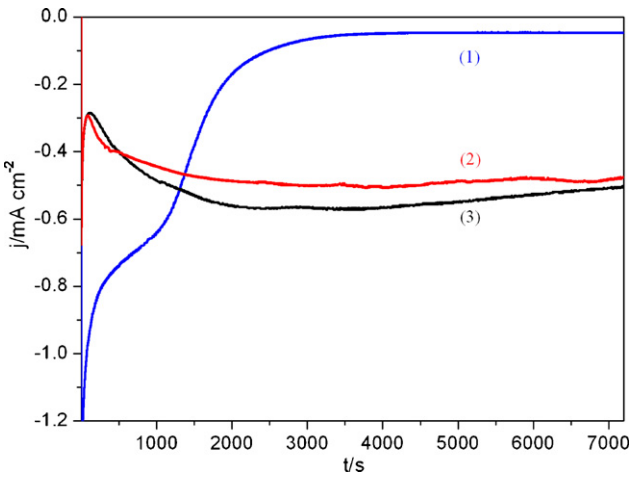

Fig. 3. Chronoamperograms obtained from: (1) 0.001 M of Sm^{3+},(2) mixed Sm^{3+} (0.8 mol%) - Ce^{3+} and (3) 0.05 M Ce^{3+}.

Firstly, the CV experiments were performed in pure $NaNO_3$ solution under different atmospheres: argon, as an inert gas, and oxygen, presented in Fig. 1 curves (1) and (2), respectively. The existence of cathodic wave under oxygen-saturated conditions, starting approximately at −0.3 V vs. SCE and reaching its maximum negative value at about −0.68 V vs. SCE, can be assigned to the electrochemical reduction of molecular oxygen, as documented in literature [21].

A change in shape of the CV curves is observed, when the CV experiment was carried out under the same oxygen-saturated conditions, but in the presence of 1 mM Sm^{3+} (pH 6), (see Fig. 1, curve 3. Therefore, it appears that the cathodic peak observed, with a maximum at −0.86 V vs. SCE, is the Sm induced one. Moreover, this electrochemical signal was found to be related to the concentration of Sm^{3+} species in the solution, as its increase from 1 to 10 mM resulted in proportional increase in the corresponding peak current. Also, the peak position shifted slightly from −0.84 V to −0.89 V vs. SCE, as the Sm^{3+} concentration increased (not shown). Our result is consistent with the previous study already reported [21].

The CV was also performed for the Ce^{3+} containing solution. Fig. 2 shows cyclic voltammograms for 0.05 M Ce^{3+}. The CV for 1 mM Sm^{3+} solution is given in parallel. In the case of Ce^{3+} containing species, the hysteresis observed during the reverse scan indicates that the electrode surface was modified during the cathodic polarization, especially in this relatively concentrated solution. This result indicates that the reduction reaction occurs rapidly. Hamlaoui et al. [25] reported a peak at −0.86 V vs. SCE for the 0.1 M cerium nitrate solutions, which was assigned to the evolution of cerium species. As this peak did not appear for 0.01 M solution, the cerium nitrate concentrations were suggested to be the reason. In our experiments, an irreversible cathodic peak was registered at −0.9 V, which is closer to the value reported in literature [16].

The above-presented results permitted to select a constant potential value for further synthesis of samaria and Sm-doped ceria films by electrochemical cathodic deposition method. The absolute value of this potential has to be higher than |0.6|V/SCE to ensure the formation of hydroxide ions in the vicinity of the working electrode. In this study, we have chosen to apply a potential of −0.8 V vs. SCE. As this potential is common for a successful deposition of Sm-based and Ce-based films, we applied this potential to the mixed solution of Sm^{3+} and Ce^{3+} nitrate components to grow the SDC film.

Fig. 3 shows the evolution of current density with time during the electrodeposition process for pure Sm-based films (curve 1) and ceria films (curve 3), as well as for SDC film prepared from the mixed Ce^{3+} and Sm^{3+} solution (curve 2).

Current-density transient curve obtained for pure samarium nitrate solution exhibits a characteristic S shape, (see curve 1, Fig. 3). Globally, there is a continuous decrease in cathodic density with time, nevertheless different distinct steps are observed. Just after the application of reductive potential, the current increases drastically. For the 0%Sm^{3+} and 0.8%Sm^{3+} solution it can be observed that over the first 1000 s, the current decreases and reaches a plateau value of about −0.65 mA cm^{-2}. The current decrease continues again towards the steady value of only −0.050 mA cm^{-2} reached after 3000 s. Such electrochemical behavior suggests that the formed Sm-layer is of low conductivity in this electrolytic medium. Ruiz et al. [21] reported previously that the formation of incipient Sm-based film partially blocked the electrode surface to the subsequent reduction of water reduction.

Chronoamperometric transient curves related to CeO_2 and SDC films both exhibit a particular shape. Actually, upon the application of the potential, the cathodic current increases, as the formation of ceria hydroxide occurs. The overall process takes about 2000 s when the current reaches the value of about −0.6 mA cm^{-2}. The second part of the process, which may be assigned to the homogenous crystal growth process, is characterized by more or less constant current-density. This shape, different from pure samaria, indicates the deposition mechanisms are different.

3.2. Morphological and compositional characterization

The Sm-based film was electrodeposited on the stainless steel substrate from 1 mM $Sm(NO_3)_3{\cdot}6H_20$ solution for 2 h. Microstructure of the as-grown film is presented in Fig. 4(a) and (b).

At first sight, the film does not seem to fully cover the surface, as bare substrate is partly visible, Fig. 4(a). The cracks observed in the film are most likely the result of dehydration of the sample. Indeed by the curvature of film patches, it is easily concluded that the cracking is the consequence of the shrinkage of deposited film, as well as the result of the shear stresses between oxide/hydroxide film and stainless steel substrate (during oxidation step or/and drying step). The presence of the cracks therefore suggests that the film contains hydroxide groups (Eq. (3)). The film appears fibrous and very porous, as can be seen in Fig. 4(b). The microstructure of the SDC sample is presented in parallel, Fig. 4(c) and (d). According to our observations, the film is quite adherent despite it is cracked on its surface, and has the same morphology as pure ceria film (not shown). However, in comparison with the pure as-grown samaria film (Fig. 4a and b), the Sm-doped ceria shows much more compact and denser morphology (Fig. 4c and d). Such morphology is suit-

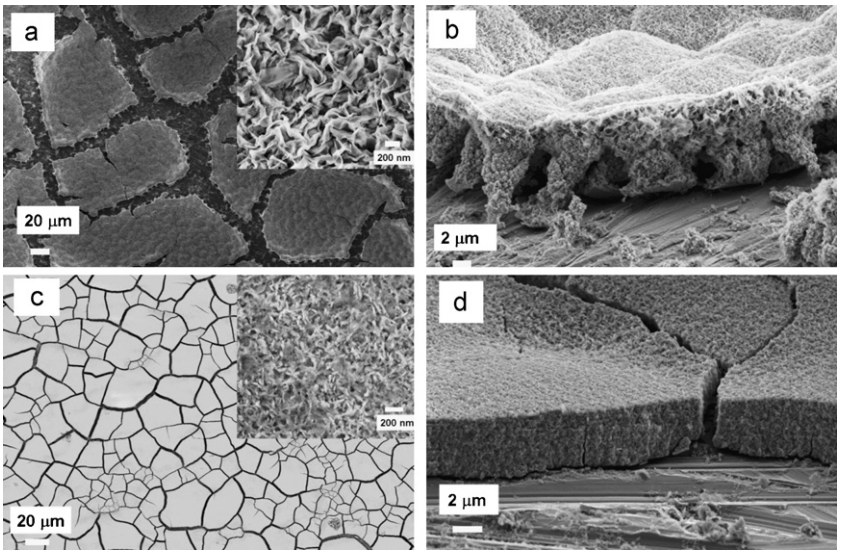

Fig. 4. Different SEM views: (a) and (c) surface views and (b) and (d) cross sectional views of as-grown Sm-based and SDC films on steel substrate, respectively.

able for protection of metallic surfaces or as thin electrolyte if ionic conductor.

The energy dispersive X-ray analysis for the SDC film was performed and the samarium and cerium quantities were measured in more than three locations throughout the specimen, in order to determine its composition accurately. The Ce signals were registered at 0.9, 4.9, and 6.0 keV, while the Sm related ones appeared at 1.1 and 5.6 keV. The use of standards allowed us to calculate the final composition as 95 at.% Ce and 5 at.% Sm.

3.3. Structural characterization and Raman spectroscopy studies

Fig. 5 illustrates diffraction patterns of as-grown Sm-based film, as well as the effect of thermal annealing on its crystallinity. As can be seen, as-deposited film shows no features of a crystallized compound (Fig. 5 curve (1)). However, after annealing at 600 °C for 1 h, the presence of cubic Sm_2O_3 was confirmed (curve 2). XRD peaks positioned at 2θ values of 28.3°, 32.8° and 47.0°, corresponding to the (2 2 2), (4 0 0) and (4 4 0) crystallographic planes, match well the standard data JCPDS 015-0813. The line width is rather narrow, suggesting that the deposited samaria is quite

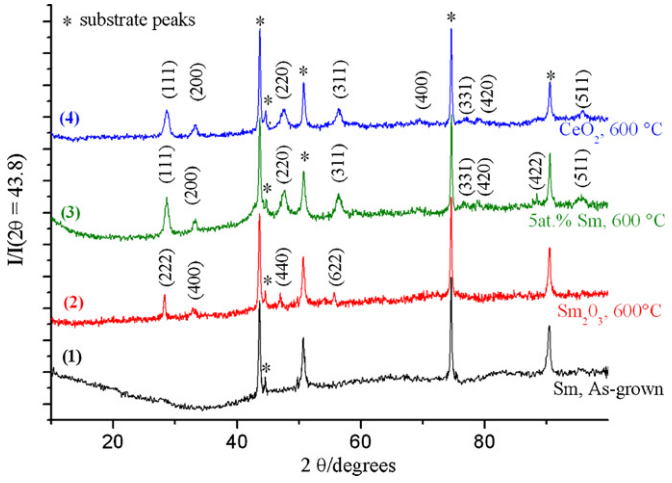

Fig. 5. X-ray diffraction patterns of: (1) as-grown Sm-films and (2) Sm-films annealed at 600 °C for 1 h; (3) The annealed SDC (5 at.%) and (4) pure ceria films annealed at 600 °C 1 h.

crystallized and the average crystallite diameter of 27 nm was calculated.

The X-ray patterns of pure ceria and 5 at.% Sm-doped ceria films, annealed at 600 °C for 1 h, are also presented in Fig. 5 (curves 3–4). According to JCPDS 34-0394, the registered peaks clearly confirm that the cubic fluorite CeO_2 phase is the compound diffracting from both films. As can be observed, XRD peak (1 1 1) is the dominant one and both films (curves 3–4, Fig. 5) exhibit a well-defined peak situated at about 28.6°. Lower intensity diffraction lines assigned to (2 0 0), (2 2 0), (3 1 1) crystallographic planes, as well as a series of lower intensity peaks, were recorded in both patterns (curves 3–4, Fig. 5). However, in comparison with pure ceria (curve (4), Fig. 5), 5 at.% Sm-containing ceria film (curve (3), Fig. 5) shows more intense peaks of narrower line-widths, indicating an increase in grain size with Sm doping. Accordingly, the average crystallite size of 10.8 and 13.5 nm was calculated for pure and doped ceria, respectively. Our result corroborates well the reported data [32].

It can be noted that in the case of Sm_2O_3, bcc structure is defined, while pure ceria crystallized in fcc structure, resulting in a slight shift of X-ray peaks. This is not observed anymore by the 5 at.% Sm-doping, concluding to the formation of a single SDC phase, with a structure close to pure ceria and not pure samaria. This result was expected due to the small amount of Sm dopant, low enough to not modify the ceria structure.

Raman spectroscopy is a versatile non-destructive technique, which can provide information about the material quality, phase and purity [37–39]. It was used to study dopant incorporation and influences the scattering of the samaria and SDC coatings. Fig. 6 illustrates the Raman spectra of the Sm-films, as grown and after annealing at 600 °C for 1 h. The peak at 1054 cm^{-1}, dominant for the as-grown sample (curve 1, Fig. 6), and the one located at 741 cm^{-1} are attributed to the internal vibration modes of nitrate ions [26]. The same band has already been reported for the as-grown ceria films when washed with water [25]. Both nitrate related peaks almost vanish (denoted as (*)) from the spectra upon annealing, curve (2).

After the thermal treatment, new peaks appear in the spectra, with a major Raman peak at 344 cm^{-1}. Our results are in accordance with the reported data [40,41], attributing this peak at 344 cm^{-1} to the F_g mode for samaria, and the two adjacent ones, at 295 and 417 cm^{-1}, to the $F_g + E_g$ and A_g mode for samaria, respectively [42]. In addition, two new bands of lower intensity were registered: a small band at 555 cm^{-1} and a wide one, but rather

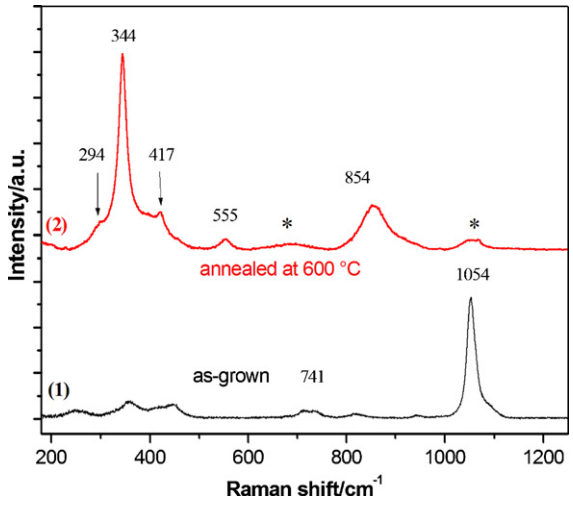

Fig. 6. Raman spectra of Sm films: (1) as-grown and (2) annealed at 600 °C.

significant, located at 854 cm^{-1}. The Raman peak at 555 cm^{-1} was evidenced as the Sm_2O_3 one [42,43], assigned to the E_g mode. Authors [40,41] presented the spectra recorded in much smaller Raman wave-number ranges than in this study. Nevertheless, it could be suggested the peak at 854 cm^{-1} to be also assigned to Sm_2O_3 [42], as similar Raman spectrum was registered for the sample electrodeposited at a potential different than $E = -0.8$ V vs. SCE.

Next, pure and Sm-doped ceria samples were studied by the Raman scattering method. It is known that CeO_2 crystallizes in the cubic fluorite-type lattice, belonging to the *Fm*3*m* space group. The Raman mode frequency at about 456 cm^{-1}, viewed as a symmetric breathing mode of the oxygen atoms around ceria atom [44–46], can be directly detected by measurements (Fig. 7). Typical Raman spectra for as-grown pure and 5 at.% Sm-doped ceria films are shown in Fig. 7(a). Both spectra are characterized by an intense band at 456 cm^{-1}, attributed to the F2g mode of Ce–O symmetric vibrations. This result agrees well with literature data [9,13,26] for non-calcined ceria particles. Although both pure ceria and SDC spectra exhibit similar shape, an increase in intensity is observed for the Sm-doped sample.

The effect of the thermal treatment on Raman spectra for pure and Sm-doped ceria samples is presented in Fig. 7(b). The high Raman intensity (Fig. 7b) measured for the strongest band in all the samples indicates a large polarizability change occurring during the vibration studies. This band is expected to be more sensitive to changes in chemical bonding [42] in the series and will be monitored to study the doping-induced effects in all the samples studied. After annealing, an increase in symmetry of the Raman band, along with a decrease in the full width at half maximum is observed. Also, the peak intensity doubles. According to Fig. 7 it is also evident that annealing produces a shift in the maximum amplitude of the Raman band towards higher wave numbers, from 456 to 465 cm^{-1}, for as-grown and annealed films, respectively. This could be related to the higher degree in crystallinity and an increase in crystallite size [47–49]. A special correlation model of this effect has been used to account for the variations in Raman line width and frequency vs. particle size by Richter et al. [48] and Viera et al. [49]. It was found that the crystallite size increases with decreasing FWHM of the Raman peaks. Our experimental observations are in accordance with previous reports [49]. Thus, we can mention that there is a correlation between the Raman FWHM (line width) and inverse particle size. Moreover, a slight Raman shift of 2 cm^{-1} towards lower wave numbers in respect to pure ceria (curve (1)), observed for SDC film, curve (2), is in agreement with [9]. Furthermore, in close vicinity of the main band, the evolution of

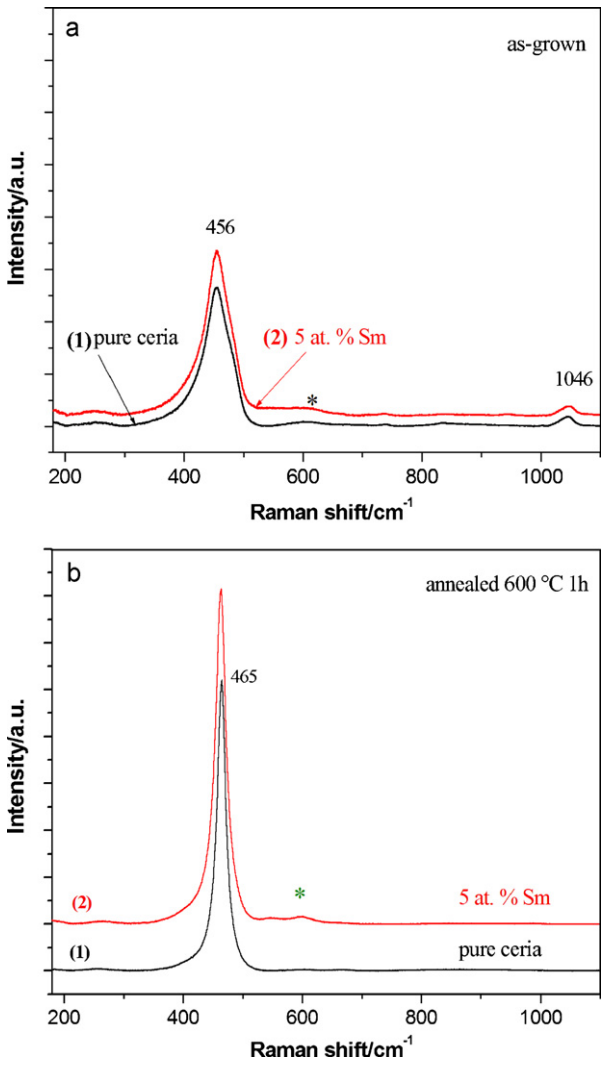

Fig. 7. Raman spectra of pure ceria and 5 at.% Sm-doped ceria films: (a) as-grown and (b) annealed at 600 °C.

a "shoulder-like" band around 600 cm^{-1} is registered. The related band, with a maximum at 600 cm^{-1}, observed in both spectra, disappears after annealing from the pure ceria spectrum, but not from 5% Sm ceria. McBride et al. [44] assigned a new, additional band, observed at about 570 cm^{-1} in spectra of doped-ceria sample, to the oxygen vacancies formed by doping with aliovalent species. Another possible explanation of the physical mechanism of this mode may be explained by the impurity centers which breaks the translational symmetry of the crystal and relax the conservation of wave vector. This may lead to scattering by phonons in the host material which has wave vector far from the zone center.

The appearance of the broad Raman band in the 500–630 cm^{-1} region is commonly considered to be a further evidence of the solid solution formed during precipitation [14,42–44,50,51]. Kosacki et al. [51] stated that the width of this band increased when the size of ceria particles decreased. These observations are in agreement with our XRD data and calculations above.

With the aim of following the evolution of the crystal structure as a function of Sm and Ce amounts, Raman spectra for films of different final compositions have been analyzed in terms of peak positions and intensities. Fig. 8 illustrates the spectra for pure ceria (curve 1) and for 5 at.% Sm-doped (curve 2), as well as for 50 at.% Sm-doped ceria films (curve 3) [34], and pure samaria films (curve 4) given in parallel for comparison (all samples were annealed at

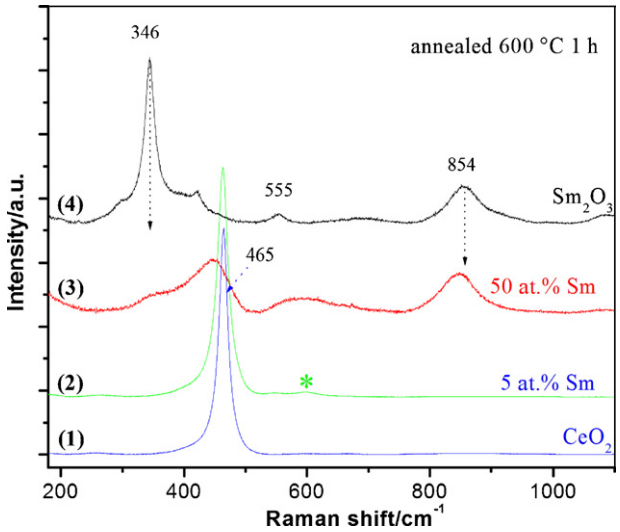

Fig. 8. Raman spectra of electrodeposited films: (1) pure ceria; (2) 5 at.% Sm-doped ceria; (3) 50 at.% Sm and 50 at.% Ce, and (4) pure samaria. All samples were annealed at 600 °C for 1 h.

600 °C, 1 h). For pure ceria film, the F2g mode of Ce–O symmetry is clearly positioned at 465 cm^{-1} [42]. However, as already discussed, the samarium presence, even at low doping level (5 at.%), produces a change in ceria Raman spectra: it shifts the first order peak to 463 cm^{-1} and gives rise to a new band positioned at around 600 cm^{-1}. For the 50 at.% Sm sample, this band becomes much more pronounced. Another wide band, in the Raman shift range from about 300 to 510 cm^{-1}, was also registered for this Sm-rich coating. This large band is apparently formed of 2 smaller ones, but distinct bands, witnessing both ceria and samaria presence in the film. However, the peak corresponding to Sm_2O_3 is not clearly defined, but present as a shoulder at around 346 cm^{-1}. As opposed, the second constituting large band, evidently relates to ceria. With an increase in samarium content from 5 to 50 at.%, there is a simultaneous decrease in cerium amount in the film, consequently, the first order ceria Raman peak shifts to much lower frequencies, from 463 to 448 cm^{-1}. The band at 854 cm^{-1} (curve 3), assigned in previous text to samaria, is also visible in the sample with 50 at.%Sm, but slightly shifted towards lower Raman frequencies.

As can be seen in Fig. 8, curves 1–3, the intensity of Raman peaks at 465 cm^{-1} increase with the Sm-doping concentration up to 5 at.%, which demonstrates that the crystal quality of the films can be improved with doping concentration of 5 at.%. However, it depressed by more Sm-doping atoms, see curve 3 for 50 at.%. These results are consistent with the XRD patterns of the investigated films. It can be deduced from Figs. 7 and 8 that doping influence the Raman peaks of ceria and SDC materials.

4. Conclusions

The samaria, ceria and Sm-doped ceria coatings were synthesized on stainless steel substrate at room temperature, by means of cathodic electrodeposition method, under potentiostatic conditions ($E = -0.8$ V vs. SCE) for 2 h. Cyclic voltammetry studies, performed for Sm^{3+} and Ce^{3+} nitrate solutions, permitted the choice of deposition potential for elaboration in order to deposit SDC films in one electrochemical conditions set.

All obtained films crystallize into cubic structure. Moreover, Sm-doping was found to contribute to the better crystallinity of ceria, proven by XRD and Raman spectroscopy. A detailed Raman analysis of as-grown and annealed samaria and SDC films is discussed. The intensity of Raman peaks at 465 cm^{-1} increase with the Sm-doping concentration up to 5 at.%, which demonstrates that the crystal quality of the films can be improved with doping concentration of 5 at.%. However, it depressed by more Sm-doping atoms, e.g. for 50 at.%. The evolution of the crystal structure is highlighted, and the change in peak position and intensity is discussed in the light of Sm and Ce content. These results are consistent with the XRD patterns of the investigated films.

Acknowledgements

This work is supported by ANR (Agence Nationale de la Recherche-France) ANR JCJC06-0131 COMICEL program. The authors are grateful to Dr. S. Delpech (LECIME-ENSCP) for access to the Raman spectrometer. Dr. Lj. Živković acknowledges CNRS for the research position and also thanks the Ministry of Science of the Republic of Serbia (Pr. No 45012). Dr. O. Lupan acknowledges the CNRS for support as an invited scientist at the LECIME-ENSCP.

References

[1] M. Primet, E. Garbowski, Catalysis by Ceria and Related Materials, Imperial College Press, London, 2002.
[2] E. Odier, Y. Schuurman, C. Mirodatos, Catal. Today 127 (2007) 230.
[3] N. Izu, W. Shin, I. Matsubara, N. Murayama, Sens. Actuators B 113 (2006) 207.
[4] S. Hiliare, X. Wang, T. Luo, R.J. Gorte, J.A. Wagner, Appl. Catal. A 215 (2001) 271.
[5] B. Daslet, P. Blennow, P. Vang Hendriksen, N. Bonanos, D. Lybye, M. Mogensen, J. Solid State Electrochem 10 (2006) 547.
[6] Z. Duan, M. Yang, Z. Hou, Y. Dong, Y. Chong, M. Cheng, W. Yang, J. Power Sources 160 (2006) 57.
[7] T. Tsai, S. Barnet, Solid State Ionics 98 (1997) 191.
[8] T. Karaca, T.G. Altinçekiç, M.F. Öksüzömer, Ceram. Int. 36 (2010) 1101.
[9] E.C.C. Souza, E.N.S. Muccillo, J. Alloys Compd. 473 (2009) 560.
[10] H. Yahiro, Y. Eguchi, K. Eguchi, H. Arai, J. Appl. Electrochem. 18 (1988) 527.
[11] B.C.H. Steele, High Conductivity Solid Ionic Conductors-Recent Trends and Applications, World Scientific, London, 1989.
[12] W. Fergus, Mater. Sci. Eng. A 397 (2005) 271.
[13] Y. Hamloui, C. Rémazeilles, M. Bordes, L. Tifouti, F. Pedraza, Corros. Sci. 52 (2010) 1020.
[14] K. Kamada, N. Enomoto, J. Hojo, Electrochim. Acta 54 (2009) 6996.
[15] L. Arurault, P. Monsang, J. Salley, R.S. Bes, Thin Solid Films 466 (2004) 75.
[16] H. Ardelean, I. Frateur, P. Marcus, Corros. Sci. 50 (2008) 1907.
[17] D.-C. Chen, W.-F. Li, W.-H. Gong, G.-X. Wu, J.-F. Wu, Trans. Nonferrous Met. Soc. China 19 (2009) 592.
[18] M.A. Arenas, J.J. de Damborenea, Electrochim. Acta 48 (2003) 3693.
[19] M. Bethencourt, F.J. Botana, M.A. Cauqui, M. Marcos, M.A. Rodriguez, Appl. Surf. Sci. 238 (2004) 278.
[20] W.F. Ng, M.H. Wong, F.T. Cheng, Mater. Chem. Phys. 119 (2010) 384.
[21] E.J. Ruiz, R. Ortega-Borges, L. Godinez, T.W. Chapman, Y. Meas-Vong, Electrochim. Acta 52 (2006) 914.
[22] J.A. Switzer, Am. Ceram. Soc. Bull. 666 (1987) 1521.
[23] I. Zhitomirsky, A. Petric, Ceram. Int. 27 (2001) 149.
[24] J. Creus, F. Brezault, C. Rebere, M. Gadouleau, Surf. Coat. Technol. 200 (2004) 4636.
[25] Y. Hamloui, F. Pedraza, C. Remazeilles, S. Cohendoz, C. Rebere, L. Tifouti, J. Creus, Mater. Chem. Phys. 113 (2009) 650.
[26] Y. Hamloui, F. Pedraza, L. Tifouti, Corros. Sci. 50 (2008) 2182.
[27] L. Arurault, B. Daffos, F.X. Sauvage, Mater. Res. Bull. 43 (2008) 796.
[28] V. Lair, A. Ringuedé, P. Vermaut, S. Griveau, Phys. Status Solidi C 5 (2008) 3492.
[29] H. Elbelghiti, V. Lair, A. Ringuedé, M. Cassir, ECS Trans. 7 (2007) 2261.
[30] L. Čerović, V. Lair, O. Lupan, M. Cassir, A. Ringuedé, Chem. Phys. Lett. 494 (2010) 237.
[31] S. Phok, R. Bhattacharya, Phys. Status Solidi A 203 (2006) 3734.
[32] S. Phok, R. Bhattacharya, P. Spagnol, T. Chaudhuri, J. Electrochem. Soc. 153 (2006) C2736.
[33] Y. Hamlaoui, L. Tifouti, C. Remazeilles, F. Pedraza, Mater. Chem. Phys. 120 (2010) 172.
[34] L. Živković, V. Lair, O. Lupan, A. Ringuedé, Thin Solid Films (2011) 245, doi:10.1016/j.tsf.2011.01.
[35] T Pauporté, E. Juanno, F. Pellé, B. Vianna, P. Aschehoug, J. Phys. Chem. C 113 (2009) 1042.
[36] A. Goux, T. Pauporté, D. Lincot, Electrochim. Acta 53 (2007) 50.
[37] O. Lupan, L. Chow, L.K. Ono, B. Roldan Cuenya, G. Chai, H. Khallaf, S. Park, A. Schulte, J. Phys. Chem. C 114 (2010) 12401.
[38] W. Limmer, Appl. Phys. Lett. 72 (1998) 2589.
[39] O. Lupan, V.V. Ursaki, G. Chai, L. Chow, G.A. Emelchenko, I.M. Tiginyanu, A.N. Gruzintsev, A.N. Redkin, Sens. Actuators B 144 (2010) 56.
[40] J.-F. Martel, S. Jandl, A.M. Lejus, B. Vianna, D. Vivien, J. Alloys Compd. 275–277 (1998) 3653.

[41] N. Dilawar, S. Mehrotra, D. Varandani, B.V. Kumaraswamy, S.K. Haldar, A.K. Bandyopadhyay, Mater. Charact. 59 (2008) 462.
[42] N. Dilawar, D. Varandani, S. Mehrotra, H.K. Poswal, S.M. Sharma, A.K. Bandyopadhyay, Nanotechnology 19 (2008) 115703.
[43] J.F. Martel, S. Jandl, B. Viana, D. Vivien, J. Phys. Chem. Solids 61 (2000) 1455.
[44] J.R. McBride, K.C. Hass, B.D. Poindexter, W.H. Weber, J. Appl. Phys. 76 (1994) 2435.
[45] W.H. Weber, K.C. Hass, J.R. Mc Bride, Phys. Rev. B: Condens. Matter Mater. Phys. 48 (1993) 178.
[46] Y. Ji, J. Liu, T. He, J. Wang, W. Su, J. Alloys Compd. 389 (2005) 317.
[47] G.W. Graham, W.H. Weber, C.R. Peters, R. Usmen, J. Catal. 130 (1991) 310.
[48] H. Richter, Z.P. Wang, L. Ley, Solid State Commun. 39 (1981) 625.
[49] G. Viera, S. Huet, L. Boufendi, J. Appl. Phys. 90 (2001) 4175.
[50] R. Torrens, N.M. Sammet, G. Tompsett, J. Electroceram. 13 (2004) 683.
[51] I. Kosacki, T. Suzuki, H.U. Anderson, P Colomban, Solid State Ionics 149 (2002) 99.